Contrib Mineral Petrol (2010) 160:279–295
DOI 10.1007/s00410-009-0477-3

ORIGINAL PAPER

Redistribution of HFSE elements during rutile replacement by titanite

Friedrich Lucassen · Peter Dulski · Rainer Abart · Gerhard Franz · Dieter Rhede · Rolf L. Romer

Received: 18 June 2009 / Accepted: 1 December 2009 / Published online: 1 January 2010

Abstract Titanite growth at the expense of rutile during retrograde hydration of eclogite into amphibolite is a common phenomenon. We investigated an amphibolite sample from the Tromsø eclogite facies terrain in Northern Norway to gain insight into the trace element distribution between rutile and titanite during incomplete resorption of the rutile by titanite. Patchy compositional zoning of Al, Ti, and F in titanite relates to the presence of a fluid with variable Ti/Al and/or F during its growth. Laser ablation ICP–MS and electron microprobe data for high field strength elements (HFSE: Nb, Zr, Ta, and Hf) of rutile resorbed by titanite indicate a pronounced enrichment of these elements in the rim of a large single rutile crystal (~8 mm) and a systematic decrease towards uniform HFSE contents in the large core. HFSE contents of smaller rutile grains (~0.5 mm) and rutile inclusions (<100 μm) in the titanite overgrowth are similar or higher than in the rims of large rutile crystals. Element profiles from the rim inward demonstrate that HFSE enrichment in rutile is controlled by diffusion. HFSE ratios in diffusion-altered rutile show systematic variations compared with the uniform core composition of the large rutile. Modelling of Zr and Nb diffusion in rutile indicates that diffusion coefficients in rutile in fluid-dominated natural systems must be considerably higher than those determined experimentally at 1 bar in dry systems. Variations of HFSE contents in the newly formed titanite show no systematic spatial distribution. HFSE ratios in titanite and the rims of rutile are different, indicating different solid/fluid distribution coefficients in these minerals. Element fractionation by diffusion into the relict rutile and during fluid-mediated growth of new titanite could substantially change the HFSE budget of these minerals and could affect their use for geochemical tracing and other applications, such as Zr-based geothermobarometry.

Keywords Rutile · Titanite · Metamorphic reaction · HFSE distribution · Nb, Zr diffusion in rutile

Communicated by J. Hoefs.

Electronic supplementary material The online version of this article (doi:10.1007/s00410-009-0477-3) contains supplementary material, which is available to authorized users.

F. Lucassen (✉) · G. Franz
Technische Universität Berlin, Fachgebiet Petrologie, ACK 9, Ackerstr. 71–76, 13355 Berlin, Germany
e-mail: lucassen@gfz-potsdam.de

F. Lucassen · P. Dulski · D. Rhede · R. L. Romer
Deutsches GeoForschungsZentrum, Telegrafenberg, 14473 Potsdam, Germany

R. Abart
Freie Universität Berlin, FB Geowissenschaften, Malteserstr. 74-100, 12249 Berlin, Germany

Introduction

Titanite ($CaTiSiO_5$) and rutile (TiO_2) are accessory minerals in a variety of metamorphic and magmatic rocks and occur as detrital minerals in sedimentary rocks. These minerals are of specific interest for geochemical tracing, because both can incorporate considerable amounts of trace elements (e.g., Deer et al. 1992; Tiepolo et al. 2002; Zack et al. 2002; Seifert and Kramer 2003; Schmidt et al. 2008). Rutile is an important carrier of high field strength elements (HFSE) and dominates, e.g., the Nb, Ta, and W budget of many rocks. It can also accommodate considerable amounts of Zr and Hf. Titanite can be enriched in rare earth elements (REE) and Sr and also contain appreciable amount of HFSE. In certain mineral paragenesis, rutile and titanite

preferentially incorporate U and/or Th and are suitable for U–Pb geochronology (e.g., Mezger et al. 1989; Frost et al. 2000). HFSE are broadly used for geochemical provenance studies in whole rocks due to their immobility during alteration processes (e.g., Pearce and Cann 1973) and have been also applied in provenance studies of rutile in clastic sedimentary rocks (e.g., Zack et al. 2004a; Meinhold et al. 2008). An increasing body of calibrations and applications use the temperature dependence of Zr incorporation in rutile and titanite for thermometry (e.g., Zack et al. 2004b; Spear et al. 2006; Watson et al. 2006; Hayden et al. 2008).

Primary trace element signatures in these minerals were acquired during crystallization at peak metamorphic conditions or during magmatic crystallization. Titanite overgrowth on rutile is a common phenomenon during retrogression of metamorphic rocks, e.g., granulite and eclogite facies rocks, and may proceed to complete consumption of the rutile. Changes induced by such secondary processes to the trace element contents of titanite and rutile are of major interest. For instance, geochronologic studies have shown that secondary titanite may inherit U–Pb signatures of the precursor rutile (Romer and Rötzler 2003; Rötzler et al. 2004). Such chemical inheritance could result in U–Pb ages that are too old and hence unrelated to the true age of titanite formation. Variable HFSE signatures in various generations of rutile are related to the pro- and retrograde reaction history of granulite and demonstrate the possible mobility of these elements in metamorphic processes (e.g., Luvizotto and Zack 2009).

The focus of this study is the HFSE distribution in titanite overgrowth and the rutile host from variably sized rutile crystals in a single sample of retrogressed eclogite. We demonstrate that the HFSE distribution pattern in the rutile was changed during the progress of rutile-consuming titanite-growth.

Sample description

The hand specimen UT (courtesy of U. Troitzsch, Australian National University; Canberra) is from the Tromsø (Norway) eclogite area (Krogh et al. 1990; Ravna and Roux 2006; Ravna et al. 2006). This amphibolite comprises Ca-hornblende (<50 vol%; some grains are slightly zoned with ^{M4}Na in cores up to 0.15 p.f.u. (p.f.u. = per formula units); rims ~0.1 p.f.u.; normalized to 23 O), plagioclase (<40 vol%; cores $An_{\sim 12}$ rims $An_{\sim 20}$), and variable, but generally small amounts of calcite, quartz, and epidote/zoisite and rare phengitic mica (Si up to 6.75 p.f.u.; normalized to 22 O). The medium grained part of the sample, which is dominated by hornblende and plagioclase, is referred to as amphibolite matrix in the following. A fine-grained aggregate of zoisite (FeO total <2 wt%) + biotite (no zoning) + plagioclase (core up to An_{20}, rim up to An_{30}) + quartz (~20 mm length) occurs in the amphibolite matrix. Rare apatite with ~4 wt% F is the only F-bearing phase. Amphibole and biotite contain negligible amounts of F. Veins at the cm scale comprise coarse-grained hypidiomorphic hornblende (similar in composition and weakly zoned as the matrix amphibole), titanite, calcite, plagioclase, and quartz. Textural relations demonstrate that the vein-related minerals represent the latest formations, because they crosscut amphibolite matrix and the fine-grained aggregate (Fig. 1a). Representative electron microprobe (EMP) analyses of the minerals are given in ATable 1 (appendix).

Metamorphic conditions in eclogite of the Tromsø area reached ~2 GPa, ~700°C (Krogh et al. 1990; Ravna and Roux 2006; Ravna et al. 2006). A possible UHP stage at ~3.3 GPa was suggested for rocks from the Tromsø area (Ravna and Roux 2006). The high Si phengite could represent a relic from the eclogite stage. A large rutile crystal of cm size (Fig. 1b) was probably part of the eclogite assemblage, because such large rutile crystals are typically observed in veins and segregations of eclogite facies rocks (e.g., Holland 1979; Thomas and Franz 1989; Selverstone et al. 1992; Gao et al. 2007). The mineral assemblages (amphibolite matrix, fine-grained aggregate, and coarse-grained veins) are tentatively assigned to the amphibolite stage in the regional evolution, which is characterized by the hydration of the eclogite rocks under amphibolite facies conditions ($P < 1.0$ GPa, $T < 700$°C; Krogh et al. 1990; Ravna and Roux 2006; Ravna et al. 2006). Titanite is of the low Al-type (Al 0.05–0.17 p.f.u; ATable 2) that is considered to be typical of amphibolite facies metamorphic conditions (Al <0.25 p.f.u; Oberti et al. 1991). Compositional variations of hornblende, plagioclase, and phengitic mica are similar to those reported in retrogressed samples by Ravna and Roux (2006) from the area. We made no further attempt to quantify metamorphic conditions in the sample that lacks garnet.

We selected two thin sections (UT1 and UT2) according to size of the rutile and fabric relations of the sample UT for detailed analyses. A large rutile crystal (UT1) is partly embedded in the amphibolite matrix and surrounded by a thin rim of poly-crystalline titanite overgrowth (~0.5 mm) and partly in contact with a large single-crystal titanite (~10 mm) obviously related to a vein (Fig. 1b, c). Variably sized rutile grains with poly-crystalline titanite (UT2) overgrowth are irregularly distributed in the amphibolite matrix (diameter of poly-crystalline titanite with rutile core up to 5 mm; Fig. 1a, d). Small round rutile grains in the titanite overgrowth are locally common and interpreted as remains of precursor rutile (Fig. 1d). The lobate boundary between titanite and rutile is a typical texture caused by the resorption of one mineral by another.

Poly-crystalline titanite commonly shows an idiomorphic crystal shape in contact with the surrounding minerals. Hornblende and plagioclase in contact with titanite show no

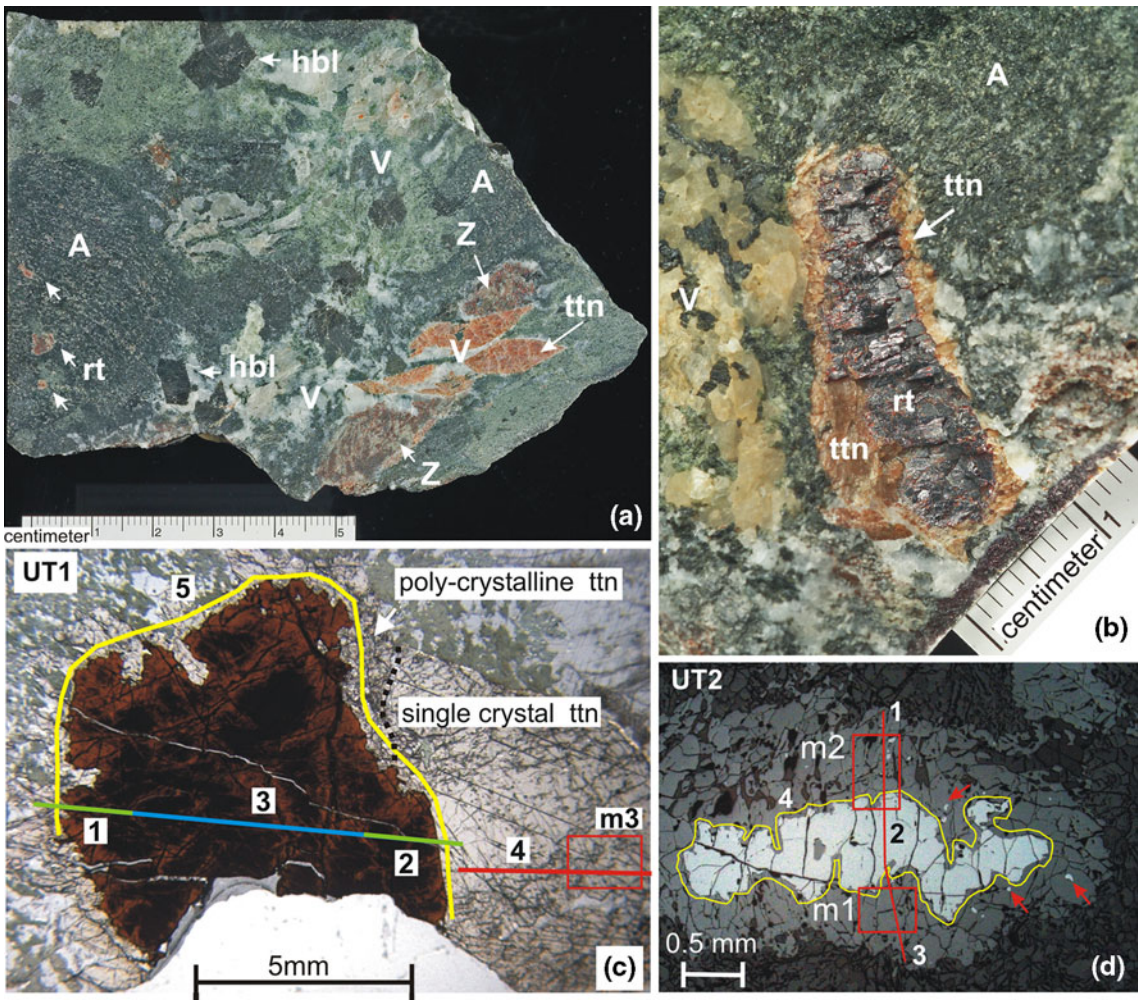

Fig. 1 **a**, **b** Photographs of the hand specimen UT, showing the appearance of rutile (rt) and the fabric relations. **a** Relation between veins (V), amphibolite matrix (A), and fine-grained biotite–zoisite plagioclase aggregate (Z). Various small rutiles with titanite (ttn) overgrowth occur in the amphibolite matrix. Large single-crystal titanite and single-crystal amphibole (hbl) occur in the veins. **b** The large rutile with titanite rim is partly embedded in the amphibolite matrix partly in contact to a vein. **c**, **d** Position of electron microprobe (EMP) and laser LA–ICP–MS analysis profiles at UT1 and UT2. Detailed information on the position of the individual LA-spots and EMP profiles is given in AFigure 1. **c** UT1, thin section (transmitted light) of the large rutile with poly-crystalline titanite overgrowth in amphibolite matrix and in contact with a large single-crystal titanite related to a vein (*broken black line*: border between the two types of titanite). m3 indicates position of element mapping in Fig. 3c; *1*, *2*, *3*, *4*, and *5* indicate profile lines. **d** UT2, polished section, reflected light of rutile with poly-crystalline titanite overgrowth in amphibolite matrix. Small rutile relicts are preserved in the titanite rim (*red arrows*). m1 and m2 denote the positions of element distribution maps in Fig. 3a and b; *1*, *2*, *3*, and *4* indicate the profile lines

indication of a hornblende and plagioclase consuming reaction. However, inclusions of hornblende, plagioclase, and minor calcite in the different titanite types point to possible contributions of these minerals to the titanite growth. There is no pervasive deformation associated with the titanite growth.

Sampling and analytical methods

Major and trace (Nb, Zr) element contents were measured with EMP along parallel lines crossing titanite overgrowth and rutile (Fig. 1). Concentrations of Nb, Ta, Zr, W, Hf, and major elements were determined by LA–ICP–MS along the EMP profiles at UT1 and UT2. In addition, points on either side of the titanite–rutile interface were measured along the contact between the two minerals by LA–ICP–MS at UT1 and UT2 (Fig. 1c, d). As much as 31 spots analyses were performed by LA–ICP–MS following the pronounced Al compositional variation in the titanite of UT2. A profile over a large single titanite crystal from a vein comprises 36 spots and follows the variable major element composition explored by EMP. Labelling and exact positions of the individual LA-spots are in the Appendix (AFig. 1). Al, Ti, and F distribution maps were obtained from different titanite crystals by EMP (Fig. 1). The positions and labelling of the individual LA-spots are

in the Appendix (AFig. 1). LA–ICP–MS and EMP analyses are given in the Appendix (ATable 2).

Chemical compositions of minerals were determined by wavelength-dispersive X-ray analysis (WDS) techniques using CAMECA SX-100 electron microprobe at the Deutsches GeoForschungsZentrum. Operating conditions were 15 kV accelerating potential, 20 nA beam current, and beam diameters of 1–2 μm. Peak counting times were 10–20 s, backgrounds were counted 5–10 s. Standards used included the following synthetic and natural minerals: topas (F), albite (Na), orthoclase (Al, Si), borazite (Cl), wollastonite (Ca), rutile (Ti), and hematite (Fe). The raw intensity data were corrected with the 'PAP' program (Pouchou and Pichoir 1988). In trace element mode, Nb concentrations at high spatial resolution were measured over the rutile–titanite interface. The concentration of Nb (Nb_2O_5 standard) was determined with a higher beam current of 100 nA and counting times of 300 s on the peak. The detection limit for Nb was ~50 ppm.

The element mapping was carried out in the WDS mode moving the stage in steps of 1–2 μm, using a beam current of 40–100 nA, and counting times of 300–500 ms per step.

Trace elements including Nb and Zr were determined by LA–ICP–MS.

Instrumentation

The GEOLAS M Pro laser ablation (LA) system (Coherent, Germany) coupled to an ELAN DRC-e ICP-MS (Perkin-Elmer/SCIEX, Canada) was used for this study at Deutsches GeoForschungsZentrum.

The LA device consists of an excimer laser (COMPex-PRO 102, Argon Fluoride, 193 nm, Coherent, Germany) with a maximum output energy of 200 mJ per pulse for repetition rates between 1 and 20 Hz, an optical beam path homogenizer to provide a homogeneous laser beam, an aperture system for variable spot sizes between 5 and 160 μm, a petrographic microscope (Olympus BX 51, Olympus, Japan), a 20 cm^3 sample cell, and a computer controlled *x*, *y*, *z*-stage. Samples can be observed through the petrographic microscope by a binocular and two objective lenses with different magnification (5- and 20-fold). During ablation, the sample image was observed continuously on a separate high-resolution monitor (20″, Sony, Japan) through a Schwarzschild objective (25-fold magnification) and a high-resolution CCD camera (D20D, Hitachi, Japan). Helium was used as carrier gas, mixed with argon as a makeup gas before entering to the plasma torch of the ICP–MS. The fully automated system is controlled by the Geolas software. The operating parameters of the laser ablation system and the ICP–MS are summarized in Table 1. The system was optimized (using NIST 610 glass standard) to achieve high sensitivity combined with low oxide formation rate (ThO/Th < 0.2%) and a U/Th ratio close to one.

Table 1 Operating parameters LA–ICP–MS

GeoLas Pro M laser ablation system	
Energy (mJ)	120–170
Energy density (J cm^{-2})	10
Repetition rate (Hz)	10
He carrier gasflow l min^{-1}	0.9
Laser spot size (μm)	24 and 44
Mode	Single hole
ELAN DRC-e ICP–MS	
ICP RF power (W)	1,400
Plasma gas flow (l min^{-1})	14
Auxiliary gas flow (l min^{-1})	1.2
Makeup gas flow (l min^{-1})	0.8
Detector	Dual
Autolens	On
Dwell time/isotope (ms)	10
Quadrupole settling time (ms)	3
Mode	Peak jump, TRA analysis
Isotopes measured	^{23}Na, ^{24}Mg, ^{27}Al, ^{29}Si, ^{42}Ca, ^{57}Fe ^{90}Zr, ^{93}Nb, ^{178}Hf, ^{181}Ta, ^{184}W

Data acquisition and reduction

LA–ICP–MS measurements for elements of interest were carried out using time resolved analysis operating in peak jump mode (one point per mass). Each measurement consisted of approximately 60 s background measurement (gas blank: laser firing, shutter closed) followed by acquiring transient signals of the analytes for 30 to 60 s depending on the spot size (sampling: laser firing, shutter open) using 10 ms dwell time and 3 ms quadrupole settling time of the ICP–MS. Each analytical batch consisted up to 20 analyses. The NIST 610 glass standard (used for external calibration) was measured twice at the beginning and twice at the end of an analytical batch using a repetition rate of 10 Hz, an energy density of 10 J cm^{-2}, and a spot size of 44 μm. Samples were measured using a repetition rate of 10 Hz, an energy density of 10 J cm^{-2}, and spot sizes of 24 μm (ttn–rt boundary) or 44 μm (core of the large rutile crystal).

For data reduction, the LOTUS 123 macro-based spreadsheet program LAMTRACE was used. A brief description of the capabilities of the program is given by van Jackson (2008), and its algorithms are described in Longerich et al. (1996). The program performs background correction, correction for instrumental drift, internal calibration, calculation of element concentrations using external calibration, and calculation of limits of detection (LOD) for each analysis. Integration intervals for gas blank

and sample were selected by the user after inspection of the individual spectra. Ca was used as internal standard for titanite and Ti for rutile. Trace element concentrations used for calibration (NIST 610) were obtained from preferred values of GeoReM database (Jochum and Nehring 2006).

Several parameters (Table 2) describe the overall system performance during the analytical runs for the determination of Zr, Nb, Hf, Ta, and W in rutile and titanite samples. U/Th ranging between 1.00 and 1.10 for 52 individual ablations of NIST 610 indicate robust conditions for complete atomization and ionization (Hattendorf et al. 2003). Count rates for 247 measured gas blanks are $\ll$10 ips (ions per second). In a day three to four analytical batches have been run. Each batch consisted of two NIST 610 ablations at the beginning and the end of a batch. To establish the typical precision on NIST 610 over a working day the two NIST 610 samples at the beginning and the end of an analytical day were used as calibration samples and the other NIST 610 samples ($n = 12$ or 16 depending on the day), measured in between, as unknowns. During 5 days of data acquisition, the precision (1 s, %) for NIST 610 varied between 0.7 and 0.9 (Zr), 0.6 and 1.0 (Nb), 0.7 and 1.2 (Hf), 0.9 and 1.4 (Ta), and 1.0 and 1.8 (W). To estimate the precision for measurements on rutile the inner core of the large crystal (UT1) was used. The precision (1 s, %) for the analysis of 36 single 44 μm spots (spacing 100 μm) was 2.5 (Zr), 2.2 (Nb), 4.4 (Hf), 3.9 (Ta), and 8.6 (W).

The determined element concentrations in the course of this study cover a wide range (Zr: 16–430 ppm, Nb: 42–830 ppm, Hf: 1–13 ppm, and Ta: 3–32 ppm, W: 0.5–580 ppm). The LAMTRACE software calculates limits of detection (LOD) for each individual analysis (single hole). LODs varied between 0.01 and 0.9 ppm for the different sample types (rutile, titanite), spot sizes (24 and 44 μm), and elements. For each analysis the ratio concentration/LOD has been calculated, clearly indicating that all determined concentrations are well above the limit of detection except for a few values found for W.

Composition of rutile and titanite

Major element compositional variations in common titanite are due to the substitution $(Al^{3+}, Fe^{3+}) + (F^{(-)}, OH^{(-)}) \leftrightarrow {}^{VI}Ti^{4+} + O^{2-}$ (e.g., Oberti et al. 1991). The Al content in the titanite in our sample varies between $\sim$0.05 and 0.17 p.f.u. (including <0.4 wt% FeO, Fe total < 0.01 p.f.u.) and is correlated with the Ti and F contents (Fig. 2). The compositional range of poly-crystalline rims and the large single-crystal is nearly identical. HFSEs (except Ti) are present only at the trace element level. Possible substitutions of Sr and rare earth elements (REE) for Ca are below the detection limit ($\approx$0.01 wt%) of the routine EMP setup. Ca and Si are near 1 p.f.u. (normalized

Table 2 Instrument performance during rutile and titanite measurements

	Unit	*n*	Zr	Nb	Hf	Ta	W
Measured isotope			Zr-90	Nb-93	Hf-178	Ta-181	W-184
Reference NIST 610	ppm		440	419	432	452	445
Gasblank	ips		≪10	≪10	≪10	≪10	≪10
Precision NIST 610, 44 μm	1 s, %	16	0.7–0.9	0.6–1.0	0.7–1.2	0.9–1.4	1.0–1.8
Precision core of large rutile	1 s, %	36	2.5	2.2	4.4	3.9	8.6
Range c rutile 24 μm	ppm	42	76–380	240–680	3.4–12	18–26	11–580
Range c rutile 44 μm	ppm	89	71–430	200–830	3.2–13	16–32	10–250
Range c titanite 24 μm	ppm	40	16–130	42–210	1.0–5.8	4.3–13	0.5–170
Range c titanite 44 μm	ppm	24	26–108	44–137	1.7–8.8	3.7–22	1–17
LOD NIST 610, 44 μm	ppm	52	0.03–0.12	0.01–0.07	0.03–0.11	0.01–0.05	0.04–0.13
LOD rutile 24 μm	ppm	42	0.2–0.6	0.07–0.50	0.1–0.8	0.07–0.20	0.3–0.9
LOD rutile 44 μm	ppm	89	0.03–0.15	0.01–0.16	0.03–0.20	0.01–0.16	0.05–0.24
LOD titanite 24 μm	ppm	40	0.04–0.58	0.02–0.31	0.06–0.48	0.01–0.18	0.08–0.88
LOD titanite 44 μm	ppm	24	0.03–0.11	0.02–0.04	0.04–0.16	0.02–0.04	0.06–0.14
c/LOD NIST 610, 44 μm		52	3,800–16,000	6,300–53,000	3,700–13,000	8,600–42,000	3,400–11,000
c/LOD rutile 24 μm		42	170–1,200	540–5,800	4–60	94–320	12–1,600
c/LOD rutile 44 μm		89	750–5,200	4,800–24,000	24–160	120–1,600	60–2,800
c/LOD titanite 24 μm		40	16–2,200	42–4,900	6–95	61–680	1–190
c/LOD titanite 44 μm		24	190–2,400	980–6,200	9–111	87–880	4–170

LOD limit of detection, *IPS* ions per second (count rate), *c* concentration, *n* number of analyses

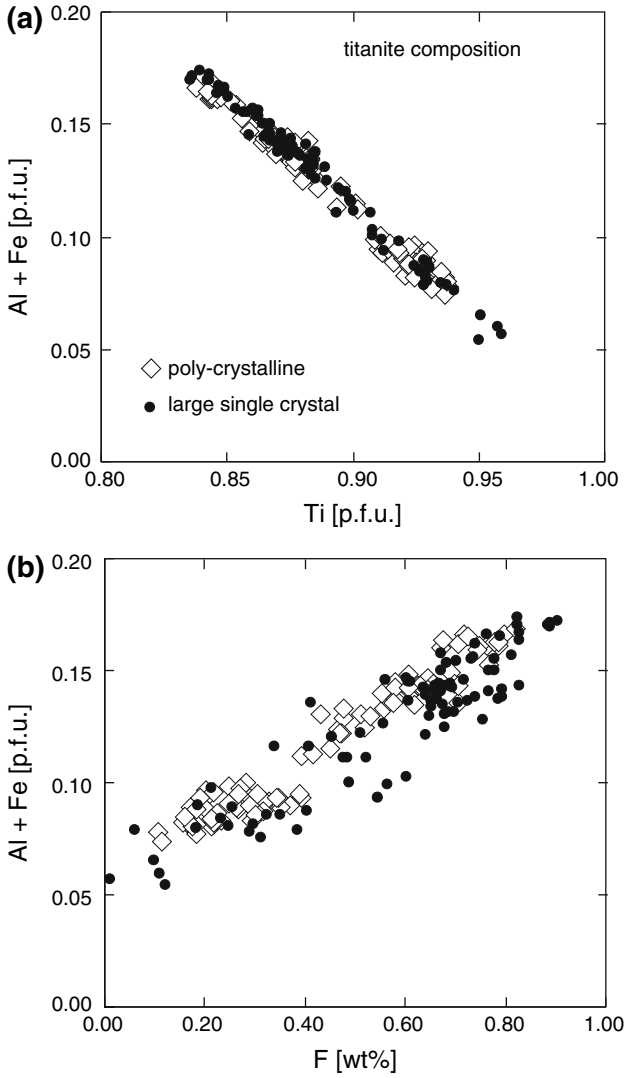

Fig. 2 **a**, **b** The variations of (Al + Fe) with Ti and F contents are similar in poly-crystalline (UT1, 2) and large single-crystal titanite (UT1). The correlation of (Al + Fe^{3+}) with F (**b**) shows larger scatter than the correlation with Ti (**a**). This is likely due to variable contribution of OH that was not determined. Fe is at the trace element level <0.01. *p.f.u.* per formula units

to 3 cations or 5 oxygens) in all analyses and no systematic variations are seen in these elements.

Distribution of variable Al (Ti, F) contents along line scans is unsystematic in both, poly-crystalline rims and large single-crystals. Element distribution maps show a complex distribution of Al in the poly-crystalline rims. Borders between patchy compositional domains are sharp; gradual transitions are less common (Fig. 3a, b). The compositional variation does not follow a concentric core to rim pattern or sector zoning. The orientation of the compositional domains could be best described as system of broad 'channels' and elongated 'islands' connecting the rutile–titanite border with the titanite–matrix contact (especially in Fig. 3b). This pattern is unrelated to the net of grain boundaries in the poly-crystalline rims (Fig. 3a). The large single-crystal titanite shows a similar, complex Al distribution (Fig. 3c).

Rutile comprises >99 wt% TiO_2 and has therefore no variation in major element concentrations. FeO total contents are <0.4 wt% and, therefore, Fe is treated as a trace element.

Trace element composition

Rutile

Nb and Zr in the large rutile UT1 (Fig. 1c; lines 1, 2, 3) increase from uniform concentrations in the extended core region to much higher values towards the interface rutile–titanite. Titanite overgrowths appear to be unzoned with respect to HFSE (Fig. 4a–c). Ta, Hf, and W concentrations show a similar distribution (AFig. 2a–c). The contents of Nb from LA–ICP–MS and EMP analyses are in good agreement (Fig. 4a, c). The Nb and Zr contents decrease in rutile UT1 in a series of rim–rim analyses rutile–titanite (Fig. 4d; Ta, Hf, and W, see AFig. 2i) from higher contents in contact with poly-crystalline to lower contents in the contact with single-crystal titanite (Fig. 1c; line 5). The Nb distribution (Fig. 1d; line 2) in the smaller rutile UT2 is bowl shaped and shows no compositional plateau (Fig. 4e). Zr concentrations show no pronounced gradient (Fig. 4e). Nb and Zr concentrations from EMP are similar or slightly lower compared with the LA–ICP–MS data (AFig. 2e). Ta and W concentrations indicate zoning, whereas the Hf distribution is more uniform and similar to Zr (AFig. 2e, f, g). The Nb, Ta, and W contents in rutile UT2 along the interface rutile–titanite (Fig. 1d, line 4) are variable in comparison with the Zr and Hf contents but show no spatial gradient (Nb, Ta in Fig. 4f; others in AFig. 2l). The HFSE contents in UT2 approach the rim concentrations of HFSE in the large rutile UT1. Small relict rutile grains (too small for LA; Fig. 1d) within the titanite overgrowth at UT2 have even higher Nb contents (Fig. 4g, h).

Titanite

The HFSE concentrations in titanite overgrowth show no (UT1, 2; Fig. 4; AFig. 2) or small systematic variations (in UT2; increase of HFSE towards one contact with rutile; Fig. 4e; AFig. 2e–g,) in lines that are perpendicular to the contact with rutile. Local strong variations in HFSE (especially Nb and W) at UT2 are attributed to small rutile inclusions in the titanite (AFig. 2e–g). In a series of analyses along the interface rutile–titanite in UT1, HFSE contents decreases from higher values in the poly-crystalline titanite to lower values in the single-crystal titanite (Figs. 1c; line 5, 4d, AFig. 2 k). The same compositional trend is obvious in the corresponding analyses of the rim of rutile (Fig. 4d,

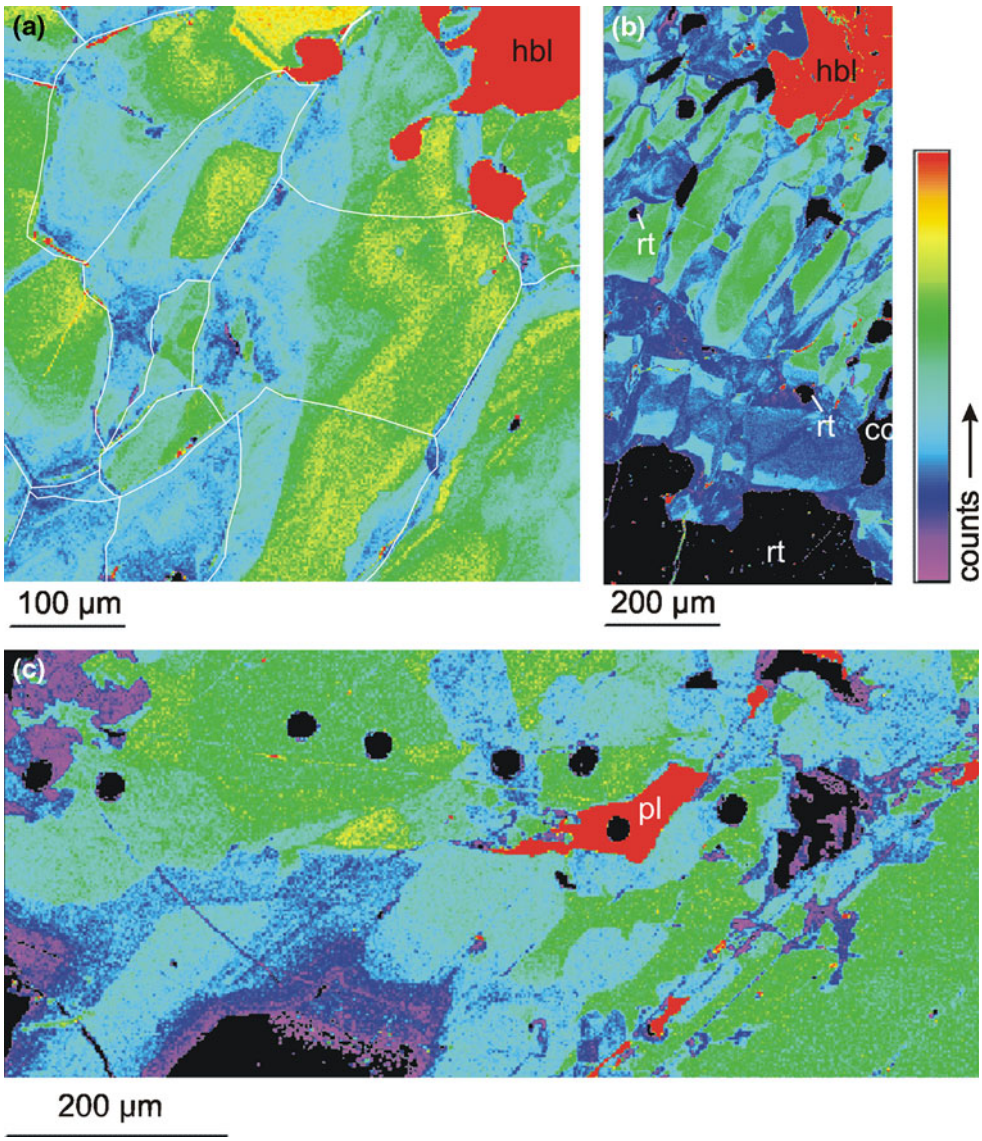

Fig. 3 Spatial distribution of Al in poly-crystalline (**a**, **b**) and single-crystal (**c**) titanite. **a** m1 in Fig. 1d; the position of the grain boundaries is indicated by *white lines*. **b** m2 in Fig. 1d; dark areas are holes, calcite, and rutile relicts; LA spots were positioned in zones of different Al contents. **c** m3 in Fig. 1c; large titanite single-crystal. The *black circles* are pits from LA–ICP–MS analysis of profile 4 (Fig. 1c). Distribution patterns of Ti and F are the same as of Al. *hbl* hornblende, *pl* plagioclase, *cc* calcite, *rt* rutile

AFig. 2j). HFSE contents of titanite along the rutile–titanite interface at UT2 shows no systematic spatial variations: the Nb, Ta, and W contents are high but variable, whereas the Zr and Hf contents are rather uniform (Fig. 4f; AFig. 2 m). Nb contents of titanite along profiles perpendicular or parallel to the boundary with small rutiles (UT2; rutiles < 100 µm; Fig. 4g, h) are not systematically elevated if compared with the average composition of titanite from areas in the overgrowth without rutile inclusions.

HFSE ratios in rutile and titanite

Average Nb/Ta, Zr/Hf, and Zr/Nb in the core of rutile UT1 are considered as the initial composition. The ratios increase along the diffusion profiles in UT1 (Table 3; AFig. 2d). Average and individual values of the ratios along the profile through rutile UT2 and along the interface rutile–titanite are in the range of the high rim compositions of UT1 (Table 3; AFig. 2 h, n). Nb/Ta and Zr/Hf in the poly-crystalline titanite are always lower than that in the adjacent rutile rims, Zr/Nb is always higher. The average Zr/Hf ratios in the poly-crystalline titanite and the uniform core of the large rutile are ~ 20 in both. Nb/Ta of the single-crystal and poly-crystalline titanite is similar, whereas Zr/Nb in the single-crystal titanite is lower that than in the poly-crystalline titanite (Table 3).

Discussion

Major element composition of the titanite

The extent of the substitution $(Al^{3+}, Fe^{3+}) + (F^{(-)}, OH^{(-)}) \leftrightarrow {}^{VI}Ti^{4+} + O^{2-}$ in titanite has been attributed to

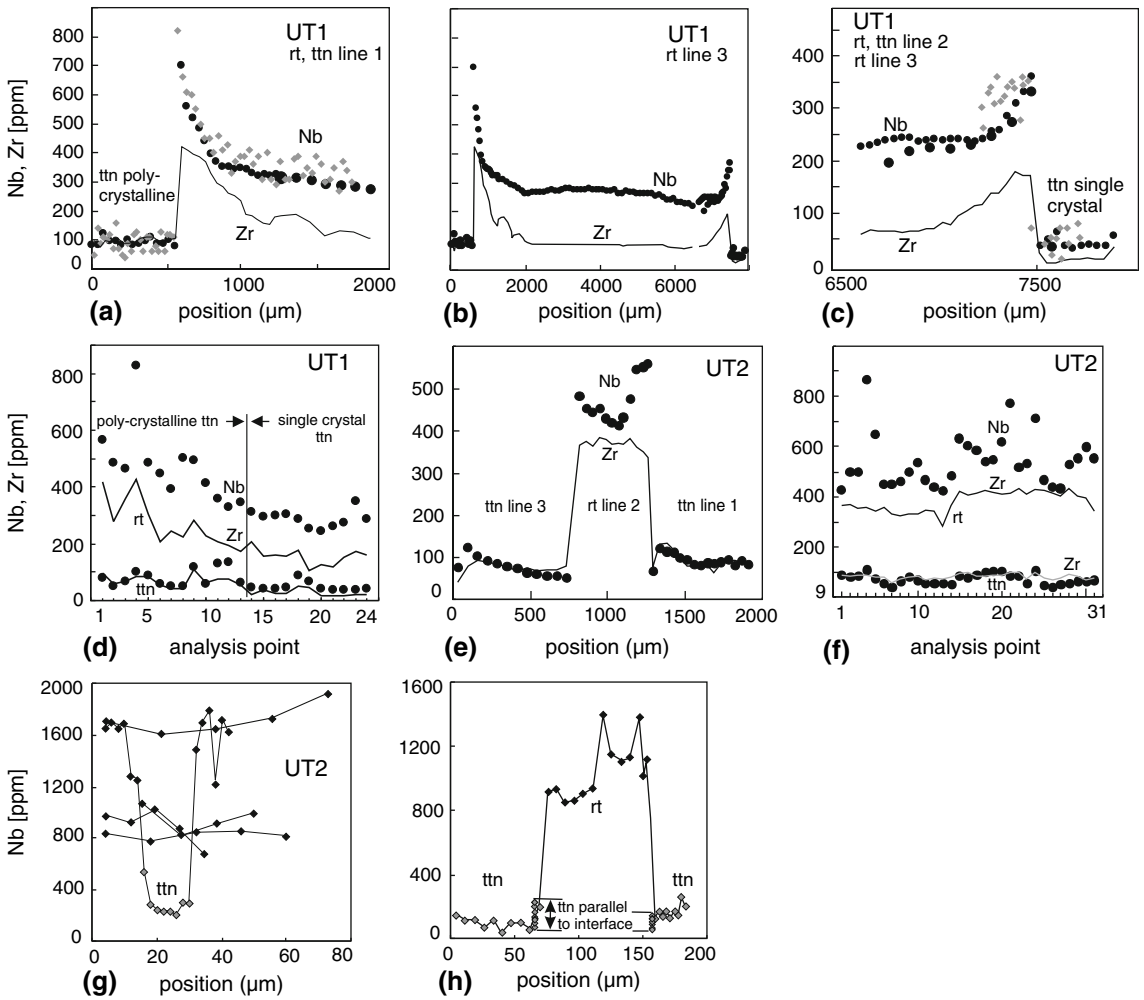

Fig. 4 Trace element contents of rutile and titanite at UT1 and UT2. **a**, **b**, **c** Large rutile crystal UT1: Nb and Zr zoning along lines 1, 2, and 3. The whole profile is in (**b**); enlargements of the transition zones rutile–titanite are in (**a**, **c**). *Large dots* refer to LA-analysis with a diameter of 44 μm, *small dots* to a diameter of 24 μm, *diamonds* to EMP analyses of Nb for the transition zone rutile–titanite at higher spatial resolution. *Solid line* for Zr refers to LA analyses, individual points omitted for clarity. Both elements show a typical diffusion-controlled zoning profile in the partially resorbed rutile crystal. The increase of Nb and Zr in rutile is less prominent towards the contact with the single crystal titanite at the right rim (**c**), compared to the poly-crystalline rim at the left side (**a**). **d** Nb and Zr contents in rutile and titanite along the interface between both minerals (line 5) measured around the large rutile UT1 (see Fig. 1c); symbols as in (**a**). Zr and Nb contents in rutile near to the poly-crystalline titanite are more variable than near to the single crystal. **e**, **f**, **g**, **h** smaller rutile crystals UT2. **e** Nb and Zr zoning of rutile and titanite along lines 1–3 and **f** along the interface between rutile and titanite (line 4); for position of the lines see Fig. 1d. **g** Nb contents of small rutile inclusions in the titanite overgrowth and **h** of small rutile inclusions and adjacent titanite perpendicular and parallel to the rutile–titanite interface. The lines indicate profiles in different grains. In small rutile relics, the Nb concentration reaches >1,700 ppm compared to ~700 ppm in the large rutile. The Nb content of titanite along the rutile/titanite interface is not or only moderately higher than in titanite away from rutile inclusions

variations of the F activity in the fluid phase and the Ti/Al ratio of the chemical environment, whereas *P* and *T* conditions are not pivotal for this substitution despite many high Al titanites are described from high *P*–low *T* conditions (e.g., Franz and Spear 1985; Enami et al. 1993; Markl and Piazolo 1999; Castelli and Rubatto 2002; Troitzsch and Ellis 2002; Seifert and Kramer 2003). The major element variability of titanite from different textural positions in the UT sample, 'early' amphibolite matrix and 'late' vein, is very similar (Fig. 2) and within the compositional range of low Al titanite (Al <0.25 p.f.u.; Oberti et al. 1991).

The diffuse to patchy zoning of the titanite with distinct compositional domains indicates that growth occurred in several stages (Fig. 3). The compositional zoning follows a 'channel-and-island' pattern in two-dimensional sections mainly perpendicular to the borders of the titanite rims. This pattern is tentatively interpreted as now closed transport paths of Ca, Si, Al, F, and OH from outside the titanite rim and Ti from the resorbed rutile. New titanite grew along the pathways and disrupted older titanite. It is reasonable to assume dissolution of rutile as the principle source of Ti, hence, a localized Ti source and local

Table 3 Average and ranges of Nb/Ta, Zr/Hf, and Zr/Nb in different profile lines

Thin section/profile	No. of analyses	Nb/Ta	1sd	Range	Zr/Hf	1sd	Range	Zr/Nb	1sd	Range
UT1 rt core line 1	47	13.7	0.4	12.7–13.5	20.3	1.1	18.4–22.8	0.30	0.02	0.28–0.35
UT1 rt rim-1 line 2	23	15.7	3.4	12.7–26.2	37.3	8.8	24.2–56.8	0.61	0.15	0.35–0.83
UT1 rt rim-2 line 3	15	13.5	1.2	11.3–16.1	24.4	4.6	18.2–33.1	0.42	0.10	0.30–0.60
UT2 rt line 2	12	20.3	1.5	18.0–22.1	37.5	3.3	32.7–43.9	0.79	0.10	0.60–0.90
UT2 rt line 4	33	22.6	4.4	15.8–31.8	34.4	2.7	28.4–39.9	0.73	0.13	0.44–0.93
UT1 ttn poly-cryst.	41	9.2	1.2	6.7–11.4	19.2	3.1	12.3–24.0	0.91	0.20	0.31–1.3
UT1 ttn single-cryst.	64	8.4	2.3	3.9–13.8	nd			0.50	0.16	0.18–0.90
UT2 ttn poly-cryst.	74	11.3	1.9	8.4–19.7	20.6	3.9	14.6–41.6	0.94	0.17	0.55–1.5
UT2 ttn line 4	26	9.6	1.8	5.8–14.3	19.5	2.0	17.5–24.7	1.2	0.25	0.80–1.7

For position of lines see Fig. 1; if no line is given titanite analyses are pooled according to the criteria single-crystal or poly-crystalline

buffering of the Ti content. The irregular zoning in titanite requires a local control (μm to mm scale) of the Ti, Al, F, and OH transport and availability. Grain boundary diffusion and enhanced element transport along grain boundaries has been shown to play an important role in material exchange between reacting minerals during metamorphism and the generation of compositional zoning (e.g., Keller et al. 2008; Prenzel et al. 2009). However, there is no relation between compositional zoning and grain boundaries in titanite with potential solid element sources, which are the partially resorbed rutile (Ti) in the core of the titanite overgrowth and the amphibolite matrix (Ca, Si, and Al) at the outer rim of the overgrowth. The variable Al contents in titanite along the interface rutile/titanite (Figs. 1d, 5 UT2 line 4) indicates the continuation of the 'channel and island' pattern at the interface. This pattern was not created or dominated by diffusion along grain boundaries. The variations in major element composition are related to the growth of the titanite. The extent of the Al–Ti substitution in all titanites is strongly correlated with the F contents (Fig. 2b), i.e., linked to the variable composition of a fluid phase. Compositional variations cannot be related to variation of the intensive parameters *P* and *T*. Such changes should cause similar spatial systematics in the composition of all types of titanite, e.g., a core–rim zoning. Further, systematic zoning in plagioclase and hornblende would be expected, which is absent, however (see above; ATable 1).

Origin of the trace elements in titanite

Rutile in mafic metamorphic rocks is the most important carrier of Nb and Ta (e.g., Zack et al. 2002; Bea et al. 2006; Schmidt et al. 2008; Luvizotto and Zack 2009). The redistribution of HFSE from the rutile during partial resorption by titanite is assessed by mass balance assuming: (1) Ti and HFSE from the resorbed rutile enter completely the titanite, (2) a uniform composition of the resorbed rutile as measured in the core of the large rutile, and (3) the averaged trace element analyses of the titanite are representative. The reaction for the average titanite composition of $CaTi_{0.89}Al_{0.11}SiO_{4.89}(F,OH)_{0.11}$ is written as 100 g rutile (TiO_2) + 78.9 g CaO + 84.5 g SiO_2 + 7.1 g Al (F, OH) = ~270 g following the approach of Gresens (1967). A dilution factor of 1/2.7 is calculated for trace elements incorporated from the resorbed rutile into the titanite. A comparison of calculated and average measured trace element compositions of titanite is made in Table 4. Nb and W in titanite are lower than the calculated values from mass balance, Ta contents are lower (UT2 lines 1, 2 and area 'a') or moderately higher. W shows systematic zoning in the core region of the large rutile with lower, but uniform contents in the outer core (AFig. 2c). The lower values are used for the calculations in Table 4; if the high values are used, the calculated W-content in titanite would be still higher (6.4 instead of 4.4). The concentration profiles of Nb, W, and Ta (in UT2) are

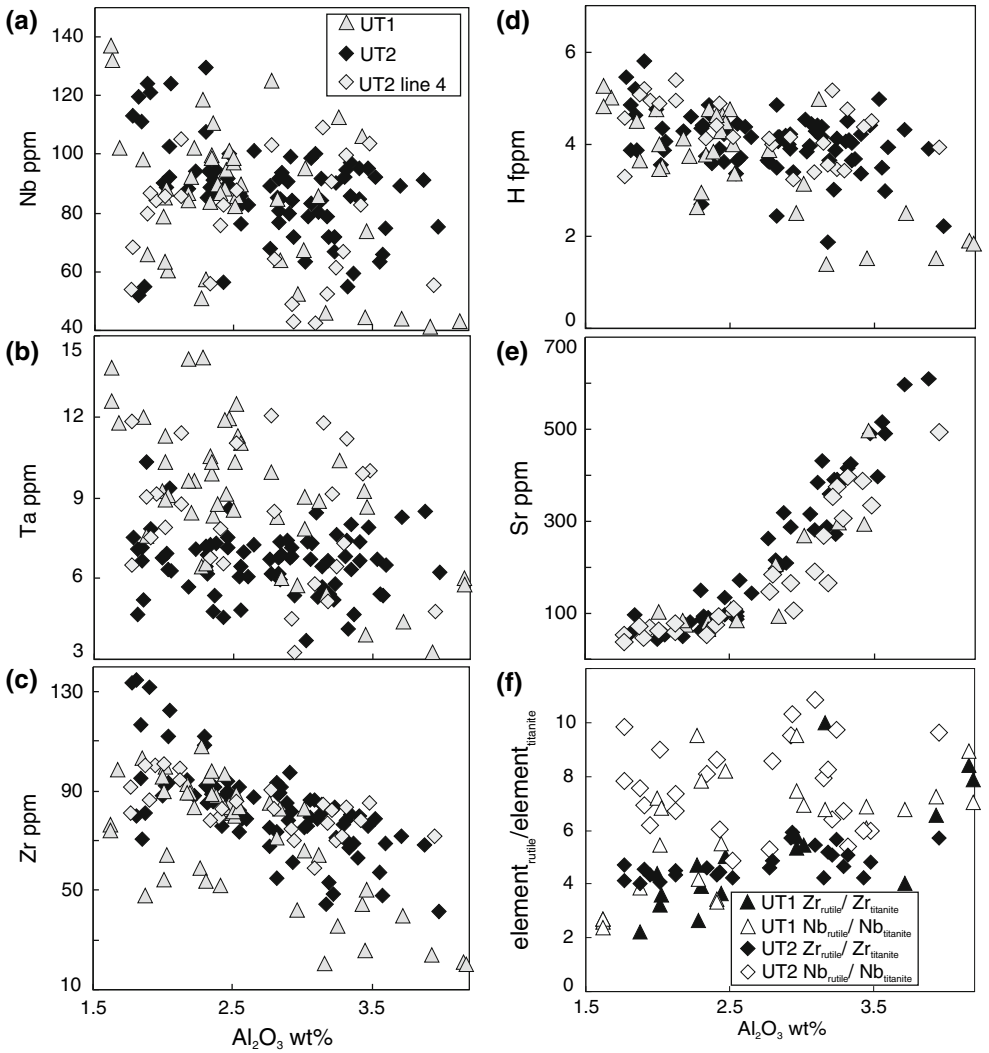

Fig. 5 a–e Relations between trace element contents (ppm) and Al_2O_3 contents (wt%) of titanite around the large rutile crystal (section UT1) and the smaller rutile (section UT2); analyses points from lines 1, 2, and 5 see Fig. 1c; for line 4 UT2, analyses along the rutile–titanite interface, see Fig. 1d. **f** Element ratios between rutile/titanite at the rutile–titanite interface; UT1 (line 5) and UT2 (line 4)

indicative for back-diffusion during resorption of rutile and formation of titanite. Average Zr and Hf contents in titanite are consistently higher by a factor of 2.3–2.9 compared with the values calculated from mass balance. Additions from external sources are required, i.e., at least for some HFSE the rutile–titanite system is open. The contents of Zr and Ta (only UT1) in titanite are correlated with the variable crystal chemistry of the titanite and decrease with increasing Al_2O_3 contents (Fig. 5b, c). Nb and Ta (only UT2) concentrations in titanite, which can be explained by mass balance with the dissolving rutile, are not correlated with the Al_2O_3 contents (Fig. 5a, b). W (not shown) and Nb, and Hf (not shown) and Zr behave similar, whereas other trace elements, e.g., the fluid mobile Sr, show a strong positive correlation with the Al_2O_3 contents of titanite (Fig. 5e).

The substitution of Nb and Ta on the Ti site in the titanite's crystal structure is described by $2Ti^{4+} \leftrightarrow (Nb, Ta)^{5+} + (Al, Fe)^{3+}$, the substitution of Zr and HF by $Ti^{4+} \leftrightarrow (Zr, Hf)^{4+}$, and the substitution of Sr on the Ca site by $Sr^{2+} \leftrightarrow Ca^{2+}$ (for a review e.g., Seifert and Kramer 2003). The influence of the Ti–Al substitution on the trace element distribution coefficients of the titanite is probably small, because substitution is limited to ~17 mol% of the Al-component in the titanite investigated here. In titanite, a change in space group from $P2_1/a$ to $A2/a$ lies somewhere between 10 and 25 mol% (Oberti et al. 1991, as observed in natural samples) or 9 and 18 mol% (Troitzsch et al. 1999, as observed in synthetic titanites) and it might well be that the change in space group is responsible for the strong change of the Sr/Al ratio at ~2.5 wt% Al_2O_3 (Fig. 5e). However, Sr generally increases with increasing Al-content, contrary to what can be expected; with increasing Al content, the Ti–Al octahedra and associated Ca polyhedra shrink (Troitzsch et al. 1999), but the ionic

radius of Sr^{2+} is larger than that of Ca^{2+}. Considering the different response of Nb–Ta and Zr–Hf to the Al-substitution (Fig. 5a–d) and the general increase of Sr with Al (Fig. 5e) we conclude that the correlation of Zr, Hf, and Sr with Al is caused by variable composition of the fluid that supplied these elements to the site of titanite growth.

The localization of the external Zr and Hf source in the UT sample is not possible, because titanite formation cannot be described by a set of reacting minerals with known compositions. Zr/Hf ratios in the core of rutile UT1 and in titanite are close to 20 (Table 4) and much lower than those of common crustal and mantle reservoirs (Zr/Hf > 30; e.g., Taylor and McLennan 1995; Weyer et al. 2003). Zr and Hf contents of bulk rocks are mainly controlled by zircon with high Zr/Hf (e.g., Zack et al. 2002; Bea et al. 2006; Schmidt et al. 2008). Zircon may react during both prograde and retrograde metamorphism in high-pressure metamorphic rocks (e.g., Tomaschek et al. 2003; Rubatto et al. 2008; Liathi and Gebauer 2009), but Na-pyroxene, amphibole, and rutile and titanite with low Zr/Hf are also potential sources of Zr and Hf during metamorphism (Zr/Hf ~ 15–25; Bea et al. 2006; Schmidt et al. 2008). The low solubility of HFSE in pure water is enhanced by addition of e.g., F, Al, and Si to the fluid and the 'immobile' HFSE can be mobilized during metamorphism (e.g., van Baalen 1993; Philippot and Selverstone 1991; Gao et al. 2007; Antignano and Manning 2008; Manning et al. 2008). The Nb and Ta budget in the titanite is dominated by the rutile, but the Nb/Ta ratio in titanite is lower (average ~8.4 to 11.3; Table 3) than that in the core of the rutile UT1 (13.7) and much lower than that in the rims of rutiles (up to 26 in UT1 and up to 36 in UT2; Table 3; AFig. 2k, n).

The HFSE released from the rutile and those introduced by an external fluid are incorporated into titanite according to their distribution coefficients, which were determined for titanite/melt (e.g., Tiepolo et al. 2002; Prowatke and Klemme 2005), but are unknown for titanite/aqueous fluid, i.e., at metamorphic temperatures. Distribution coefficients for Nb between rutile/fluid are in the order of 100 to 200 and appear to increase with decreasing P and T (Brenan et al. 1994; Stalder et al. 1998; for rutile/aqueous fluid). A rough estimate for the distribution coefficient is made here from the measured Nb contents, assuming that rutile and titanite were in equilibrium with the same fluid. The outer rim composition of the rutile at the scale of a LA-spot is taken as a minimum estimate of HFSE contents. The HFSE variation of titanite in contact with rutile is not significantly different from the variation elsewhere in the titanite (Table 3, Fig. 5a–d). The average ratio between $Nb^{rutile}/Nb^{titanite}$ along the contact large rutile–titanite UT1 is 6.4 ± 2 (1sd). The ratios are similar at the contacts poly-crystalline titanite–rutile and large single-crystal titanite–rutile, despite the variation in absolute trace element contents (Fig. 4d). The average ratio between $Nb^{rutile}/Nb^{titanite}$ at UT2 along the contact rutile–titanite is 7.7 ± 1.6 (1sd). Distribution coefficients titanite/fluid could be about a factor of ~6 to 7 smaller than rutile/fluid distribution coefficients (Brenan et al. 1994; Stalder et al. 1998). Estimated titanite/fluid distribution coefficients of ~15 to 30 are considerably higher than distribution coefficients for titanite/melt that vary between ~1 and 7 depending on the composition of the dry melt (Prowatke and Klemme 2005). The average $Zr^{rutile}/Zr^{titanite}$ of ~4.7 ± 0.6 (1sd) reflects the relative uniform contents of Zr in rutile and titanite at UT2, whereas the average

Table 4 Results of mass balance for HFSE between titanite and rutile

	Calculated titanite composition	Average titanite compositions					
		UT1 Line 1	UT1 Line 5 poly-crystalline	UT1 Line 5 single-crystal	UT2 Lines 1,3	UT2 Area 'm2'	UT2 Line 4
Nb (ppm)	97.8	94.3	81.6	89.0	84.0	91.2	76.0
Zr (ppm)	29.3	89.0	69.6	41.6	83.9	82.2	83.2
Ta (ppm)	7.2	10.3	9.5	12.0	6.5	6.7	8.2
Hf (ppm)	1.4	4.3	4.1	nd	4.2	3.9	4.3
W (ppm)	4.4	3.5	4.3	1.9	3.5	3.7	3.1
Nb_{cal}/Nb_{mea}		1.04	1.20	1.10	1.16	1.07	1.29
Zr_{cal}/Zr_{mea}		0.33	0.42	0.70	0.35	0.36	0.35
Ta_{cal}/Ta_{mea}		0.70	0.75	0.60	1.10	1.08	0.87
Hf_{cal}/Hf_{mea}		0.33	0.35	nd	0.35	0.37	0.34
W_{cal}/W_{mea}		1.26	1.02	2.37	1.26	1.21	1.43

Calculated (cal)/measured (mea) values >1 indicate that the possible HFSE contribution from the consumed rutile is greater than the measured average contents of the respective titanite; values <1 indicate that the average content of titanite is not completely explained by the contribution from the rutile. Positions of lines and area m2 in Fig. 1c, d; for the calculation procedure and assumptions see text

$Zr^{rutile}/Zr^{titanite}$ of 5.3 ± 2.3 is more variable at UT1 (Fig. 5f; AFig. 2i, j, l, m). The positive correlation between $Zr^{rutile}/Zr^{titanite}$ and Al_3O_3 (Fig. 5f) of UT1 (line 5) and UT2 (line 4) is caused by the dependence of Zr contents in titanite on variable Al-content. This and correlations between $Nb^{rutile}/Nb^{titanite}$ and the variable Nb contents in rutile and titanite preclude the precise determination of equilibrium partitioning coefficients for trace elements between rutile–titanite–fluid despite the similarities between the average calculated values for UT1 and UT2. One intrinsic problem to establish equilibrium for trace element exchange between the two minerals is that we investigate an incomplete reaction under participation of a fluid. Dissolution of the rutile must not occur at the same time and rate along the entire interface (see the lobate interface). Equilibrium trace element distribution between rutile and titanite could be local with variable concentrations of e.g., Nb released from the rutile. The irregular distribution of the rutile hosted elements Nb, W, and Ta in titanite could be a result from such small scale equilibrium. Furthermore, a fluid phase could disseminate trace elements before equilibrium is attained. The generally low Nb contents in titanite around the small high Nb rutile could be an example for such disequilibrium (Fig. 4h).

Secondary trace element zoning by volume diffusion in large rutile UT1

The most conspicuous feature of the HFSE distribution in the large rutile (Fig. 1c) is the incorporation of HFSE (Fig. 4a–c; AFig. 2) in the rims of rutile. The systematic increase of the Nb, Zr, Hf, and W concentrations in rutile towards the contact with the titanite overgrowth (Fig. 4a–c; AFig. 2) suggests that they must have propagated into the rutile by volume diffusion. An inherited zoning is precluded. Similar element distribution patterns are known from resorbed garnet with increase e.g., of Mn in the rim of garnet (e.g., Grant and Weiblen 1971; Tuccillo et al. 1990). The underlying process here is back-diffusion of elements released from the garnet during partial resorption of the garnet by a mineral phase with low distribution coefficients for the respective elements. Nb, W, and—with restrictions—Ta of the UT sample show a positive difference between calculated contents from mass balance with the core of the large rutile and average measured contents in titanite. These elements are available for back-diffusion into rutile, whereas additional Zr and Hf must be supplied from an external source to explain the Zr and Hf contents of the titanite (Table 4) and the zoning of the rutile. The trace element enrichment towards the rim of the rutile occurred during partial resorption of rutile by titanite. It is important to note that the variable trace element concentrations in titanite show no systematic distribution across the overgrowth rim along profiles perpendicular to its borders. There is, however, some systematic variation in trace element concentrations along the titanite–rutile interface UT1 (profile 5; Fig. 4d; AFig. 2i, j, k). The trace element concentrations in the outermost rutile and in the adjacent portions of the titanite overgrowth are weakly correlated suggesting trace element partitioning between rutile–fluid–titanite in local domains. The variability can be tentatively assigned to compositional gradients between the growth regime of the single-crystal titanite in the vein and the poly-crystalline titanite in the amphibolite matrix (Fig. 1).

The second end-member scenario is that trace element enrichment occurred after formation of the titanite overgrowth, in which case the trace element budget would have been dominated by the external fluid source. Although we consider this case as unlikely (absence of systematic zoning between inner and outer interface of the titanite overgrowth) it is used as a theoretical end-member scenario for model calculations.

For the scenario where trace element exchange took place after the replacement reaction had occurred, the trace element concentrations within rutile can be modelled as a function of distance z from the titanite–rutile interface and time t (Crank 1975)

$$C(z,t) = C_\infty + (C_0 - C_\infty)\mathrm{erfc}\left(\frac{z}{2\sqrt{Dt}}\right), \quad (1)$$

where C_∞ is the background trace element concentration in rutile (plateau concentration in the core region), C_0 is the trace element concentration in the outermost rutile, i.e., at the titanite–rutile interface, and D is the diffusion coefficient of the respective trace element in rutile. Equation (1) describes tracer diffusion in the half space $z \geq 0$ with constant concentration C_0 at $z = 0$ and assuming an initially homogenous concentration, C_∞, of the trace element everywhere in the rutile. Note that the model profile only depends on the product Dt, and it is only this combination of parameters that can be extracted from fitting the model curve to the observed trace element concentration profiles.

If trace element exchange between rutile and its environment took place simultaneously to the replacement of rutile by titanite, the propagation of the titanite–rutile replacement front into the rutile must be taken into account. If during replacement Ti was transferred from the rutile into the titanite quantitatively, this would imply that one mole of rutile was replaced by one mole of titanite, and because of the differences in molar volumes of the two phases ($V_{ttn}/V_{rt} \sim 3$), the volume of the newly formed titanite would be about three times the volume of consumed rutile. Given this volume change, the observed width of the rim of titanite overgrowth is about three times

as wide as the distance d that the replacement front would have propagated from the original matrix-rutile interface into the rutile. Such a scenario would imply addition of Ca and Si components to the reaction site via a fluid that was present along the grain boundary network.

For the scenario that Ti was conserved at the reaction front, the distance that the replacement front propagated into the rutile is estimated at $z = 200$ μm, based on an average thickness of 600 μm of the titanite overgrowth around the profile 1 in UT1 (Fig. 6). From petrographic evidence it appears feasible that some of the Ti was lost from the reaction site and was incorporated into large titanite crystals, which formed in nearby veins. If 50, 75 or 90% of the Ti were lost from the reaction site, then the replacement front would have propagated for distances of $z = 400$, 800 and 2,000 μm, respectively, into the rutile grain. Such scenarios, are however, rather unlikely, because they would imply unexpectedly high mobility of Ti. Nevertheless, we will consider the scenarios, where no Ti and where 90% of the Ti liberated during the dissolution of rutile are lost from the reaction site as end-member scenarios for estimating the time scale of reaction from rim width.

Lacking any detailed information on the mechanism and the rate of the replacement of rutile by titanite, we resort to the most simple model scenario that the titanite–rutile replacement front propagated into the rutile at a constant velocity. Such a scenario is compatible with interface-reaction controlled replacement, a mechanism which is very likely in the fluid saturated environment, which is inferred from petrographic evidence. We assume that the propagation of the front was slow compared to re-distribution of the trace elements by diffusion within the rutile, so that diffusion profiles will develop in front of the migrating interface, which will be "compressed" compared to the profiles that develops in a setting with fixed geometry. Eventually, a steady state concentration profile is established within the rutile, which can be described by

$$C(z,t) = C_\infty + (C_0 - C_{\mathrm{ttn}}) \exp\left(-\frac{v}{D} z\right), \qquad (2)$$

where C_{ttn} is the concentration of the trace element in the titanite overgrowth, and v is the velocity at which the reaction front propagates into the rutile (Jackson 2004), D and z have the same meanings as in Eq. (1). Equation (2) describes diffusion into the half space $z \geq 0$ from a source at $z = 0$, where the strength of the source is related to the difference in the trace element concentrations between rutile and titanite, and constant trace element partitioning is implied between rutile and titanite at the replacement front. Note that the model concentration profiles only depend on the ratio $\kappa = \frac{v}{D}$, and only this ratio can be obtained from a fit of the model curve to observed concentration data.

Both models were fitted to the trace element profiles, which were observed in rutile UT1, using the concentrations given in Table 5 as the initial and boundary conditions. A comparison of model curves and the observed concentration profiles is given in Fig. 6; the dashed and solid lines represent the "fixed geometry" and the "moving interface" models, respectively. Fitting of the "moving interface" model (Eq. 2) yields an estimate for the ratio $\kappa = v/D$ of 5×10^{-3} μm for Nb and 2.5×10^{-3} μm for Zr. Fitting of the "fixed geometry" model (Eq. 1) yields an estimate for Dt, which is 1.7×10^{-7} m for Nb and 3.9×10^{-7} m for Zr. Given that diffusion of Nb and Zr occurred simultaneously and the diffusion time t was the same for both elements, the difference in the estimated Dt by a factor of five indicates that also D_{Zr} and D_{Nb} were different by a factor of five. Similarly, based on the notion that the velocity v of interface migration was similar for Zr and Nb, it is inferred from the difference of the parameter $\kappa = v/D$ estimated from Zr and Nb by a factor of two that D_{Zr} and D_{Nb} were different by a factor of two, if the process is described correctly by the "moving interface" model. The "fixed geometry" and the "moving interface" models represent two end-member scenarios. We can thus conclude that the observed trace element profiles constrain the respective tracer diffusion coefficients to $2 \leq D_{\mathrm{Zr}}/D_{\mathrm{Nb}} \leq 5$ for any feasible diffusion scenario.

Applying the experimentally determined Arrhenius parameters given in Table 6 to a reaction temperature of 600°C the tracer diffusion coefficients D_{Zr} and D_{Nb} for Zr and Nb evaluate at 6.6×10^{-25} m^2/s and 1.2×10^{-21} m^2/s, respectively. This large difference in Zr and Nb tracer diffusion coefficients is incompatible with our analysis of the Zr and Nb concentration profiles observed in rutile U1, which yields $2 \leq D_{\mathrm{Zr}}/D_{\mathrm{Nb}} \leq 5$. Based on the "fixed geometry" model these tracer diffusion coefficients would imply unrealistically long diffusion times on the order of 7.6 billion years for Zr and more realistic diffusion times of 830,000 years for Nb. If a reaction temperature of 700°C is adopted then D_{Zr} is 7.3×10^{-24} m^2/s and D_{Nb} is 3.7×10^{-20} m^2/s, and the diffusion times obtained are 684 million years and 27,000 years for Zr and Nb, respectively.

Noting that $z = vt$, the time required to grow the titanite rim is obtained from $t = z/\kappa D$. The relations between the durations obtained from the observed thickness of the titanite overgrowth and the Nb and Zr tracer diffusion coefficients are shown in Fig. 7. If a Nb tracer diffusion coefficient of 1.2×10^{-21} m^2/s (600°C) is applied, we obtain a reaction time of 1.57 million years for the scenario of zero Ti loss and a time estimate that is by a factor of 10 larger for the 90% Ti loss; any realistic scenario for the behaviour of Ti must lie between these two end-member cases. Note that the "moving interface" model yields

Table 5 Trace element concentrations used in diffusion modelling

	Zr	Nb
C_∞ (ppm)	79	275
C_0 (ppm)	440	500
C_{ttn} (ppm)	90	95

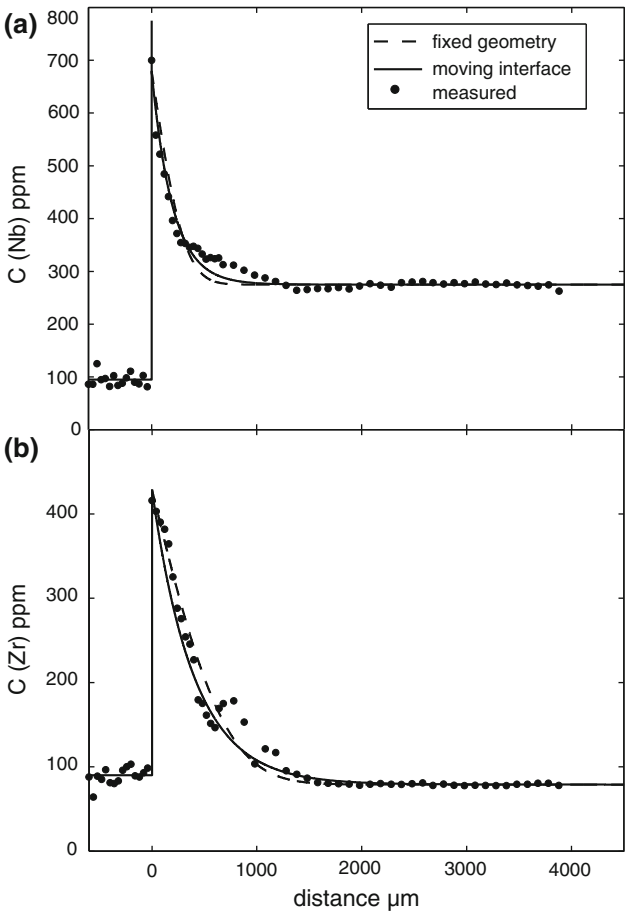

Fig. 6 Comparison of model curves for the "fixed geometry" model (*dashed lines*) and the "moving interface" model (*solid lines*) with measured concentrations (*black dots*; LA–ICP–MS data) for Nb (**a**) and Zr (**b**); the "moving interface" model yields an estimate for the ratio $\kappa = v/D$ of 5×10^{-3} for Nb and 2.5×10^{-3} for Zr; the "fixed geometry" model yields an estimate for $(Dt)^{1/2}$, which is 1.7×10^{-7} m for Nb and 3.9×10^{-7} m for Zr, see the text for discussion of these results

Table 6 Tracer diffusion coefficients for Nb after Sheppard et al. (2007) and Zr after Cherniak et al. (2007)

	D0 (m^2/s)	Ea (kJ/mol)	References
Nb	4.7×10^{-7}	244	Sheppard et al. (2007)
Zr	9.8×10^{-15}	170	Cherniak et al. (2007)

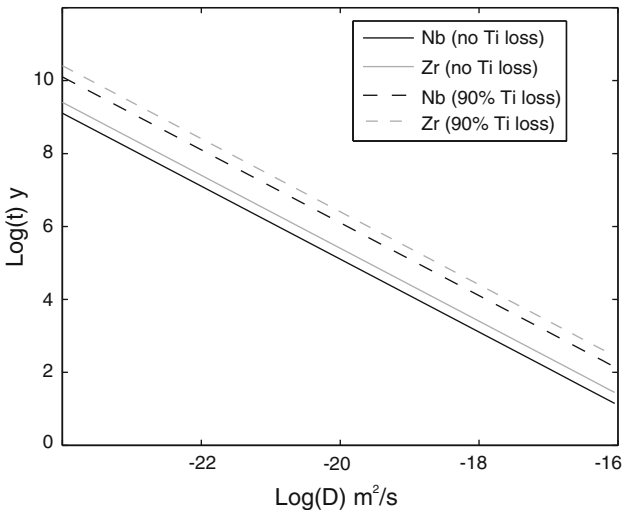

Fig. 7 Relation between estimated duration of replacement reaction and tracer diffusion coefficients of Nb and Zr; *solid lines* are for the scenario where no Ti is lost from the reaction site, *dashed lines* are for the scenario where 90% of the titanium is lost from the reaction site, *black lines* are for Nb and *grey lines* are for Zr

longer reaction times than the "fixed geometry" model. For a given set of tracer diffusion coefficients, the time estimates differ by a factor of about two for the case that Ti is conserved at the reaction site and by a factor of about 20 for the case that 90% is lost from the reaction site. The time estimates obtained from the Zr concentrations based on D_{Zr} calculated for a reaction temperature of 600°C are 1.9 and 19 billion years, respectively. For a reaction temperature of 700°C the time estimates obtained from Nb concentrations are 34,000 and 340,000 years for Ti conservation and 90% Ti loss, respectively. The time estimates obtained from Zr concentrations are 173 million years and 1.79 billion years for the two scenarios of Ti behaviour.

Given that Nb and Zr exchange occurred simultaneously, the large discrepancy between the time estimates obtained from the Zr and Nb concentration profiles suggest that the two sets of experimental data (Table 6) for D_{Zr} by Cherniak et al. (2007) and for D_{Nb} by Sheppard et al. (2007) are not compatible with each other and, at least the data by Cherniak et al. (2007) appear to be inappropriate for analysing the problem at hand. The experiments of Sheppard et al. (2007) were done at 1 bar in air, i.e., at oxygen fugacities, that are far beyond those expected for the case at hand. The experiments of Cherniak et al. (2007) were also done at 1 bar under dry conditions and at different oxygen fugacities. Cherniak et al. (2007) did not find any dependence of the tracer diffusion coefficients of Zr and Hf on f_{O2}. If time scales of 10^3 to 10^6 years are taken as a conservative estimate for the feasible range of durations of the replacement reaction, then the tracer diffusion

coefficients of Zr and Nb in rutile must have been on the order of 10^{-17} to 10^{-21} m^2/s. This is well within the range of Sheppard et al.'s (2007) Nb tracer diffusion coefficients, but at least by a factor of 10^3 faster than what is obtained for D_{Zr} (Cherniak et al. 2007). This discrepancy may be due to the fact that trace element exchange between rutile and its environment took place at relatively high pressures of several hundred MPa and under the presence of an aqueous fluid. This may have greatly enhanced the volume diffusion within rutile. The presently available data on Zr tracer diffusion in rutile seem to be inappropriate to describe diffusion controlled exchange at high water fugacity. Once such data become available, Zr and Nb concentration profiles might be used to constrain rates of replacement reactions and trace element exchange. Even though diffusion modelling of trace element profiles in rutile does not provide reliable time constraints on replacement and exchange, there are interesting inferences that can be made from this analysis and other observations on the rutile–titanite composition in this sample.

The extent of concentration changes in the outermost portions of the rutile and the distance over which the diffusion fronts move into the rutile are different for Zr, Nb, Hf, and W. As a consequence the trace element ratios show systematic variations in the outermost 500 to 1,000 μm of the large rutile grain (Table 3, Fig. 4a–c; AFig. 2). If rutile relics are smaller than about 1 to 2 mm, this implies that the original trace element signature may have been completely obliterated. From our analysis we infer that irrespective of whether trace element exchange took place during partial resorption of rutile and back-diffusion (Nb, W, and Ta) or was influenced by the composition of an external fluid during partial replacement of rutile by titanite, the trace element signature of rutile may be substantially altered by fluid mediated exchange at moderate temperatures even in grains of up to millimetre size. The variable enrichment of HFSE in smaller rutile grains of UT2 (Fig. 4e, f, g, h) is likely due to this effect.

Concluding remarks

Secondary variations of HFSE signatures in partially resorbed rutile are caused by diffusion into the rutile. Compositional zoning of major and trace elements in the new titanite is spatially not related to the rutile and reflects growth of the titanite under the variable supply of Al and F (Fig. 3). Zr and Hf contents and other trace elements in the titanite are related to the mineral chemistry. Nb, W, and Ta contents in titanite are variable, but unrelated to mineral chemistry. The ranges of Nb, W, and Ta in titanite along the interface rutile–titanite and in titanite distant from the interface are similar.

Nb and Ta contents of the rock are likely controlled by rutile. The Nb/Ta ratio is, however, compared with the ratio in titanite, higher in the core of the rutile UT1 and much higher in the rims of the large rutile UT1 and throughout the smaller rutile UT2. The low Nb/Ta in titanite could be controlled by different diffusivities of Nb (fast) and Ta (slow) during back-diffusion of these elements into the rutile. Dohmen et al. (2009) describe much lower diffusivities for Ta than for Nb in rutile in their experimental work. Considering that Zr/Hf in the core of the rutile UT1 and in the titanite overgrowth are ~20, the high Zr/Hf in the rim of rutile UT1 and in rutile UT2 were caused by different diffusivities of Zr and Hf. In the case of Zr/Hf diffusion into rutile, no pronounced effect of element fractionation by diffusion on the Zr/Hf in the titanite could be inferred. This is in accordance with our assumption of Zr/Hf control by an external fluid with Zr/Hf of ~20 that likely buffered the Zr and Hf composition in titanite.

Zr and Hf were fluid-mobile during the evolving replacement of rutile by titanite. The mobility of Nb, W, and Ta is difficult to constrain, considering that only rutile may control the whole rock budget of these elements after peak-metamorphism. The relations of the differences in Nb/Ta between the core of the large rutile, the rim of the rutile, and the titanite open a local perspective of Nb and Ta distribution (=low mobility). HFSE mobility during metamorphism from variable rutile compositions related to the reaction history of the rocks has been described by Luvizotto and Zack (2009). Zr/Hf and Nb/Ta remain unchanged in these samples, which point to bulk redistribution of HFSE. In the UT sample, changes of the presumable primary HFSE ratios in the core of the rutile are restricted to a diffusion profile in the rim. HFSE in the rim are likely controlled by variable diffusivities of the HFSE.

The newly grown titanite does not inherit the HFSE characteristics of the precursor rutile, but HFSE ratios are changed due to HFSE fractionation during back-diffusion (Nb/Ta) and influx of Zr and Hf from external sources. Thus, the HFSE characteristics of titanite cannot be used straightforward as an indicator whether rutile is the precursor mineral (which would be highly desirable for screening titanite to be used for U–Pb dating for derivation from rutile to avoid possible inheritance of the U–Pb systematics of rutile by titanite; e.g., Romer and Rötzler 2003).

Detection of diffusion-induced changes of HFSE signatures in rutile depends on the grain size, i.e., the preservation of the diffusion profile, and could pass unnoticed in small grains (Fig. 4). HFSE partitioning between rutile and titanite also affects the composition of titanite. This represents a drawback for the interpretation of individual rutile (or titanite) grains in terms of Zr-in-rutile or titanite-based geothermometry (e.g., Zack et al. 2004b; Tomkins et al. 2007; Hayden et al. 2008) or sediment provenance

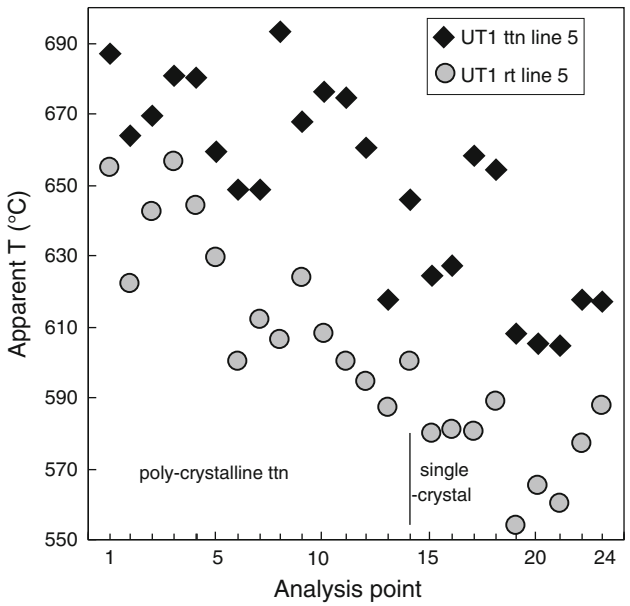

Fig. 8 Zr-in-rutile and -titanite based thermobarometry (Tomkins et al. 2007; Hayden et al. 2008) for the large rutile crystal (section UT1). The apparent (zircon is not in the paragenesis) temperatures are based on the analyses of titanite–rutile pairs, which were measured along the interface between rutile and titanite. They vary strongly from 550°C to 695°C. The positions of the analysis points 1–25 correspond to the laser spots jn25-c03 to jn25-e18 in AFigure 1a. The apparent temperatures were calculated for an assumed pressure of 0.5 GPa

(e.g., Zack et al. 2004a; Meinhold et al. 2008). In the UT sample, requirements for equilibrium distribution of Zr in rutile and titanite according to the thermometer calibrations are not given. Apparent temperatures from Zr-in-rutile and Zr-in-titanite along the interface titanite–large rutile (UT1; Fig. 1c line 5) systematically decrease by ~90°C from the contact with poly-crystalline titanite to the contact with the single-crystal titanite (Fig. 8). The compositional gradient reflected by the apparent temperatures is certainly not induced by changing temperatures during titanite growth and Zr diffusion into the rutile.

Acknowledgments We are grateful to Dr. Ulrike Troitzsch for providing the sample, who in turn thanks Prof. Erling Krogh Ravna and the Geology Department of the University of Tromsø for logistical support during the field work. Constructive and exhaustive reviews by Frank Spear, Thomas Zack, and Armin Zeh improved the manuscript and are grateful acknowledged. The study was supported by DFG grant DR 744/3-1 in the framework of the research group FOR 741 'Nanoscale processes and geomaterials properties'. We thank our colleagues of FOR 741 for stimulating discussions.

References

Antignano A, Manning CE (2008) Rutile solubility in H_2O, H_2O–SiO_2, and H_2O–$NaAlSi_3O_8$ fluids at 0.7–2.0 GPa and 700–1000°C: Implications for mobility of nominally insoluble elements. Chem Geol 255:283–293

Bea F, Montero P, Ortega M (2006) A LA-ICP-MS evaluation of Zr reservoirs in common crustal rocks: implications for Zr and Hf geochemistry and zircon-forming processes. Can Mineral 44:693–714

Brenan JM, Shaw HF, Phinney DL, Ryerson FJ (1994) Rutile-aqueous fluid partitioning of Nb, Ta, Hf, Zr, U and Th: implications for high field strength element depletions in island-arc basalts. Earth Planet Sci Lett 128:327–339

Castelli D, Rubatto D (2002) Stability of Al- and F-rich titanite in metacarbonate: petrologic and isotopic constraints from a polymetamorphic eclogitic marble of the internal Sesia Zone (Western Alps). Contrib Mineral Petrol 142:627–639

Cherniak DJ, Manchester J, Watson EB (2007) Zr and Hf diffusion in rutile. Earth Planet Sci Lett 261:267–279

Crank J (1975) The mathematics of diffusion, 2nd edn. Oxford University Press Inc., New York, p 414

Deer WA, Howie RA, Zussmann J (1992) An introduction to rock-forming minerals. Longmans Scientific and Technical, 696 p

Dohmen R, Marschall H, Ludwig T (2009) Diffusive fractionation of Nb and Ta in rutile. Geochim Cosmochim Acta 73(Suppl 1):A297

Enami M, Suzuki K, Liou JG, Bird DK (1993) Al-Fe^{3+} and F-OH substitutions in titanite and constraints on their P-T dependence. Eur J Mineral 5:219–231

Franz G, Spear FS (1985) Aluminous titanite (sphene) from the eclogite zone, south-central Tauern window, Austria. Chem Geol 50:33–46

Frost BR, Chamberlain KR, Schumacher JC (2000) Sphene (titanite): phase relations and role as a geochronometer. Chem Geol 172:131–148

Gao J, John T, Klemd R, Xiong X (2007) Mobilization of Ti–Nb–Ta during subduction: evidence from rutile-bearing dehydration segregations and veins hosted in eclogite, Tianshan, NW China. Geochim Cosmochim Acta 70:4974–4996

Grant JA, Weiblen PW (1971) Retrograde zoning in garnet near the second sillimanite isograde. Am J Sci 270:281–296

Gresens RL (1967) Composition-volume relationships of metasomatism. Chem Geol 2:45–65

Hattendorf B, Latkotczy C, Günter D (2003) Laser ablation-ICP-MS. Anal Chem 75:341A–347A

Hayden LA, Watson B, Wark DA (2008) A thermobarometer for sphene (titanite). Contrib Mineral Petrol 155:529–540

Holland TJB (1979) High water activities in the generation of high pressure kyanite eclogites from the Tauern Window, Austria. J Geol 87:1–27

Jackson KA (2004) Kinetic processes: crystal growth, diffusion and phase transitions in materials. Wiley VCH, Wertheim, 403 p

Jackson S (2008) LAMTRACE data reduction software for LA-ICP-MS. Mineralogical Association of Canada, Short Course Series, vol 40, pp 305–307

Jochum KP, Nehring F (2006) NIST 610: GeoReM preferred values (11/2006). GeoReM http://georem.mpch-mainz.gwdg.de

Keller L, Wirth R, Rhede D, Kunze K, Abart R (2008) Asymmetrically zoned reaction rims: the key to assess grain boundary diffusivities and growth rates related to natural diffusion controlled mineral reactions. J Metamorph Geol 26:99–120

Krogh EJ, Andresen A, Bryhni I, Broks TM, Kristensen SE (1990) Eclogites and polyphase P–T cycling in the Caledonian uppermost allochthon in Tromsø, northern Norway. J Metamorph Geol 8:289–309

Liathi A, Gebauer D (2009) Crustal origin of zircon in a garnet peridotite: a study of U-Pb SHRIMP dating, mineral inclusions and REE geochemistry (Erzgebirge, Bohemian Massif). Eur J Mineral 21:737–750

Longerich HP, Jackson SE, Günther D (1996) Laser ablation-inductively coupled plasma-mass spectrometric transient signal data acquisition and analyte concentration calculation. J Anal At Spectrom 11:899–904

Luvizotto GL, Zack T (2009) Nb and Zr behaviour in rutile during high-grade metamorphism and retrogression: an example from the Ivrea–Verbano Zone. Chem Geol 261:303–317

Manning CE, Wilke M, Schmidt C, Cauzid J (2008) Rutile solubility in albite-H_2O and $Na_2Si_3O_7$-H_2O at high temperatures and pressures by in situ synchrotron radiation micro-XRF. Earth Planet Sci Lett 272:730–737

Markl G, Piazolo S (1999) Stability of high-Al titanite from low pressure calcsilicates in light of fluid and host-rock composition. Am Mineral 84:37–47

Meinhold G, Anders B, Kostopoulos D, Reischmann T (2008) Rutile chemistry and thermometry as provenance indicator: an example from Chios Island, Greece. Sediment Geol 203:98–111

Mezger K, Hanson GN, Bohlen SR (1989) High-precision U-Pb ages of metamorphic rutile: application to the cooling history of high-grade terranes. Earth Planet Sci Lett 96:106–118

Oberti R, Smith DC, Rossi G, Caucia F (1991) The crystal chemistry of high-aluminum titanites. Eur J Mineral 3:777–792

Pearce JA, Cann JR (1973) Tectonic setting of basic volcanic rocks determined using trace element analysis. Earth Planet Sci Lett 19:290–300

Philippot P, Selverstone J (1991) Trace-element-rich brines in eclogite veins: implications for fluid composition and transport during subduction. Contrib Mineral Petrol 106:417–430

Pouchou JL, Pichoir F (1988) A simplified version of the 'PAP' model for matrix correction in EPMA. In: Newbury DE (ed) Microbeam Analysis-1988. San Francisco Press, San Francisco, pp 315–318

Prenzel J, Abart R, Keller L (2009) Complex chemical zoning in eclogite facies garnet reaction rims: the role of grain boundary diffusion. Mineral Petrol 95:303–313

Prowatke S, Klemme S (2005) Effect of melt composition on the partitioning of trace elements between titanite and silicate melt. Geochim Cosmochim Acta 69:695–709

Ravna EJK, Roux MRM (2006) Metamorphic evolution of the Tønsvika eclogite, Tromsø Nappe—evidence for a new UHPM province in the Scandinavian Caledonides. Int Geol Rev 48:861–881

Ravna EJK, Kullerud K, Ellingsen E (2006) Prograde garnet-bearing ultramafic rocks from the Tromsø Nappe, northern Scandinavian Caledonides. Lithos 92:336–356

Romer RL, Rötzler J (2003) Effect of metamorphic reaction history on the U–Pb dating of titanite. In: Vance D (ed) Geochronology: linking the isotopic record with petrology and textures. Geological Society, pp 147–158

Rötzler J, Romer RL, Budzinski H, Oberhänsli R (2004) Ultrahigh-temperature granulites from Tirschheim, Saxon Granulite Massif, Germany: P-T-t path and geotectonic implications. Eur J Mineral 16:917–937

Rubatto D, Müntener O, Barnhorn A, Gregory C (2008) Dissolution-reprecipitation of zircon at low-temperature, high-pressure conditions (Lanzo Massif, Italy). Am Mineral 93:1519–1592

Schmidt A, Weyer S, John T, Brey GP (2008) HFSE systematics of rutile-bearing eclogites: New insights into subduction zone processes and implications for the earth's HFSE budget. Geochim Cosmochim Acta 73:455–468

Seifert W, Kramer W (2003) Accessory titanite: an important carrier of zirconium in lamprophyres. Lithos 71:81–98

Selverstone J, Franz G, Thomas S, Getty S (1992) Fluid variability in 2 GPa eclogites as an indicator of fluid behavior during subduction. Contrib Mineral Petrol 112:341–357

Sheppard LR, Atanacio AJ, Bak T, Nowotny J, Prince KE (2007) Bulk diffusion of niobium in single-crystal titanium dioxide. J Phys Chem 111:8126–8130

Spear FS, Wark DA, Cheney JT, Schumacher JC, Watson EB (2006) Zr-in-rutile thermometry in blueschists from Sifnos, Greece. Contrib Mineral Petrol 152:375–385

Stalder R, Foley SF, Brey GP, Horn I (1998) Mineral-aqueous fluid partitioning of trace elements at 900–1200°C and 3.0–5.7 GPa: new experimental data for garnet, clinopyroxene, and rutile, and implications for mantle metasomatism. Geochim Cosmochim Acta 62:1781–1801

Taylor SR, McLennan SM (1995) The geochemical evolution of the continental crust. Rev Geophys 33:241–265

Thomas S, Franz G (1989) Kluftminerale und ihre Bildungsbedingungen in Gesteinen der Eklogitzone/Südvenedigergebiet (Hohe Tauern, Österreich). Mitt Österr Geol Ges 81:167–188

Tiepolo M, Oberti R, Vannucci R (2002) Trace-element incorporation in titanite: constraints from experimentally determined solid/liquid partition coefficients. Chem Geol 191:105–119

Tomaschek F, Kennedy A, Villa I, Ballhaus C (2003) Zircon from Skyros, Cyclades, Greece—recrystallisation and mobilisation of zircon during high pressure metamorphism. J Petrol 44:1977–2002

Tomkins HS, Powell R, Ellis DJ (2007) The pressure dependence of the zirconium-in-rutile thermometer. J Metamorph Geol 25:703–713

Troitzsch U, Ellis DJ (2002) Thermodynamic properties and stability of AlF-bearing titanite $CaTiOSiO_4$–$CaAlFSiO_4$. Contrib Mineral Petrol 142:543–563

Troitzsch U, Ellis D, Thompson J, Fitz-Gerald J (1999) Crystal structural changes in titanite along the join TiO–AlF. Eur J Mineral 11:955–965

Tuccillo ME, Essene EJ, van der Pluijm BA (1990) Growth and retrograde zoning in garnets from high-grade metapelites: implications for pressure-temperature path. Geology 18:839–842

Van Baalen MR (1993) Titanium mobility in metamorphic systems: a review. Chem Geol 110:233–249

Watson EB, Wark DA, Thomas JB (2006) Crystallization thermometers for zircon and rutile. Contrib Mineral Petrol 151:413–433

Weyer S, Münker C, Mezger K (2003) Nb/Ta, Zr/Hf and REE in the depleted mantle: implications for the differentiation history of the crust–mantle system. Earth Planet Sci Lett 205:309–324

Zack T, Kronz A, Foley SF, Rivers T (2002) Trace element abundances in rutiles from eclogites and associated garnet mica schists. Chem Geol 184:97–122

Zack T, von Eynatten H, Kronz A (2004a) Rutile geochemistry and its potential use in quantitative provenance studies. Sediment Geol 171:37–58

Zack T, Moraes R, Kronz A (2004b) Temperature dependence of Zr in rutile: empirical calibration of a rutile thermometer. Contrib Mineral Petrol 148:471–488